John von Neumann Institute for Computing

Ab Initio Simulation of Free and Supported Cluster

Michael Moseler

published in

NIC Symposium 2004, Proceedings,
Dietrich Wolf, Gernot Münster, Manfred Kremer (Editors),
John von Neumann Institute for Computing, Jülich,
NIC Series, Vol. **20**, ISBN 3-00-012372-5, pp. 181-190, 2003.

© 2003 by John von Neumann Institute for Computing
Permission to make digital or hard copies of portions of this work for personal or classroom use is granted provided that the copies are not made or distributed for profit or commercial advantage and that copies bear this notice and the full citation on the first page. To copy otherwise requires prior specific permission by the publisher mentioned above.

http://www.fz-juelich.de/nic-series/volume20

Ab Initio Simulation of Free and Supported Clusters

Michael Moseler

Faculty of Physics, University of Freiburg
Herrmann-Herder-Str. 3, 79104 Freiburg, Germany
Fraunhofer-Institute for Mechanics of Materials
Wöhlerstr. 11, 79108 Freiburg, Germany
E-mail: mos@iwm.fraunhofer.de

The electronic and geometric structure of free and supported clusters are studied within an ab inito framework by solving the Kohn-Sham equations of density functional theory (DFT) for the electrons and Newton's equation of motion for the atoms. An efficient and accurate numerical parallel implementation of the Kohn-Sham solver using a plane wave representation for the kinetic energy calculations and a real space grid for the potential energy evaluations permits structural minimisation as well as first principle molecular dynamics simulations of clusters with up to 20 atoms. An additional code for linear response calculations based on time-dependent DFT has been developed and applied to the optical response of clusters. In this paper, we report on thermal broadening mechanisms in the optical and photoelectron spectra of sodium clusters, relativistic effects in coinage metal clusters and on softlanding of Pd nanoclusters on MgO(001).

1 Introduction

The term *cluster* describes small particles made out of about three to 10^5 atomic constituents of one kind (or sometimes of a few species). Cluster physics studies the size evolution of physical and material properties bridging the gap from atomic and molecular to solid-state physics[1]. The electronic density of states of such finite systems is strongly discretized causing variations in structural, thermodynamical, optical, magnetic and catalytic properties. Consequently, clusters cannot simply be considered as scaled-down solids. In fact every atom counts rendering clusters (particularly the smaller ones) self-contained physical objects with properties that differ in many cases from that of atoms and solids. Recent development in nanotechnology utilizes this unique features in order to construct novell (so called) cluster assembled materials. For instance, cluster-polymer blends might be used as car coatings or serve as basic component of plastic solar cells[2].

The last two decades have seen major advances in experimental cluster physics resulting in the ability to produce measurable quantities of size selected clusters in free molecular beams[1] and on well defined supports[3]. Experimental analysis tools like mass spectrometry, photoelectron and optical spectroscopy, scaning tunneling and atomic force microscopy provide valuable finger prints of the structural properties of nanoclusters. However, experimental cluster science still lacks the possibility to directly explore and assign cluster geometries and dicriminate between possible isomers. Up to now, the comparison of experimental spectra with theoretical computations based on a test set of nuclear configurations represents the only realistic way to infer cluster structures. This development has been assisted by the progress in computer hardware and computational chemistry allowing the numerical investigation of free and supported clusters constisting of more than a dozend atoms as well as supporting surface models composed by almost 100 atoms[4].

In this context, the work horse of large scale quantum chemistry namely Kohn's density functional theory[5,6] plays a dominant role since it reduces the complicated many electron

system of the cluster to a more tracktable picture of single electrons in the mean field of the other electrons resulting in a 3D eigenvalue equation, the so called Kohn-Sham (KS) equation. For large systems, the KS equations can be solved with great accuracy and efficiency using a plane wave basis for the single electron wave functions[7]. However, the required memory and CPU speed still exceeds modern serial hardware and thus massive parallel computing is the only way to solve the KS equations for a large number of electrons, e.g. for the softlanding of Pd_{13} on MgO(001) in ref. 4 grids of the order of 200 grid points in each dimension were required for approximatelly 200 KS orbitals resulting in a memory consumption of several Gbyte and consumed tenthousands of CPU hours (a generous computer grant from NIC Jülich).

This contribution is organised as follows. First, we give some theoretical and numerical details of the special method used for the density functional calculations[7]. Than, its usefullness and explanatory power is demonstrated for a representative set of application namely the finite temperature dynamics of sodium cluster cations[8] and anions[9] and the thermal broadening effects in the corresponding optical and photoelectron spectra (section 3), striking effects in the dimensionality and structure of small Ag and Au clusters[10] (section 4) and the deposition dynamics and final structures of Pd clusters interacting with a typical MgO(001) surface defect, namely an F-center (section 5)[4].

2 The Born-Oppenheimer-Spin-Density-Molecular-Dynamics-Method

As mentioned in the introduction, we look for the solution of the Kohn-Sham equation for the electrons

$$\left(-\frac{1}{2}\nabla^2 + v_{eff,\sigma}(\mathbf{r}) \right) \phi_{i,\sigma}(\mathbf{r}) = \epsilon_{i,\sigma}\phi_{i,\sigma}(\mathbf{r}). \tag{1}$$

Here the $\phi_{i,\sigma}$ are a set of a single particle electronic wave function, $\epsilon_{i,\sigma}$ their energies and the effective potential is given by $v_{eff,\sigma}(\mathbf{r}) = v(\mathbf{r}) + \int d^3r' n(\mathbf{r'})/|\mathbf{r}-\mathbf{r}'| + v_{xc,\sigma}(\mathbf{r})$. The electron density n of the system as the central quantity of DFT derives from the occupied KS orbitals $n(\mathbf{r}) = \sum_{i,\sigma}^{occ} |\phi_{i,\sigma}(\mathbf{r})|^2$. In order to make the computations less expensive only chemical active electrons are considered and therefore a pseudo potential v is used for the confinement of the valence electrons representing the influence of the naked ions and the core electrons[13]. The so called exchange-correlation potential v_{xc} takes into account many body effects that are not included in the classical Coulomb field $\int d^3r' \frac{n(\mathbf{r}')}{|\mathbf{r}-\mathbf{r}'|}$ in the above equation. It is treated in the framework of the local density approximation (LDA) and improved by generalized gradient corrections[14]. The spin of the system is explicitely taken into account by calculating the wave functions of both spin manifolds $\sigma = \uparrow, \downarrow$. For more details on DFT, the reader is refered to standart text books[6].

The method for the numerical solution of eq. (1) utilizes the Born-Oppenheimer-local-spin-density-molecular-dynamics (BO-LSD-MD) approach of Barnett and Landman[7] and benefits from the fact that the differential operator $-\frac{1}{2}\nabla^2$ is a simple multiplication by $-\frac{1}{2}k^2$ for the Fourier transform $\phi_{\mathbf{k}}$ of the wave function. An iterative Block-Davidson eigenvalue solver only needs the action of the hamiltonean $-\frac{1}{2}\nabla^2 + v_{eff}$ onto a wave function and therefore a dual space technique treating the kinetic energy in Fourier and the potential energy part in real space provides a very efficient scheme to solve eq. (1). A domain decomposition of both spaces and an efficient parallelisation of the fast fourier

transform (FFT) conecting k- and real space results in a very good parallel efficiency on massive parallel machines like a Cray T3E. The FFT is also used to calculate the Coulomb field $\int d^3r' \frac{n(\mathbf{r}')}{|\mathbf{r}-\mathbf{r}'|}$ since it satisfies Poissons equation which is algebraic and thus easily solvable in k-space. For more details on the numerical aspects of the method see ref. 7.

After the solution of the KS equations, the forces on the ions are calculated employing the Hellmann-Feynman-Theorem[6] and the molecular dynamics of the respective system can be studied with very high accuracy. In certain cases where finite temperature infomation are needed a Langevin thermostat is used in order to simulate a canonical ensemble.

The extension of the KS scheme into the time domain results in a so called time-dependent (TD) DFT and allows for an investigation of electronic systems interacting with light. Thus, the optical properties of materials can be explored by solving the TD KS equations[11] with an additional TD external dipol field resulting in an eigenvalue problem for the resonance frequencies ω_I (see also ref. 12)

$$\sum_{kl}((\epsilon_i-\epsilon_j)^2\delta_{ik}\delta_{jl}+4\sqrt{(\epsilon_i-\epsilon_j)(\epsilon_k-\epsilon_l)}K_{ij,kl})F_{I,kl}=(\omega_I)^2F_{I,ij}$$

with the coupling matrix

$$K_{ij,kl}=\int d^3r_1 d^3r_2\,\phi_i(\mathbf{r}_1)\phi_j(\mathbf{r}_1)[\frac{1}{r_{12}}+\delta(\mathbf{r_{12}})\frac{\partial v_{xc}(n(\mathbf{r}_1))}{\partial n(\mathbf{r}_2)}]\phi_k(\mathbf{r}_2)\phi_l(\mathbf{r}_2).$$

Note, that we restricted ourselves to spin compensate systems. As in the statinory case the LDA is employed for v_{xc} resulting in a time-dependent LDA description (TDLDA)[11]. Note, that the index pairs ij and kl span the particle-hole space i.e. i and k represent hole states whereas j and l denote occupied orbitals. The optical oscillator strength for the transistion ω_I is given by an eigenvector weighted superposition of KS dipol matrix elements

$$f_I=\frac{4}{3}\sum_{\nu=1}^{3}\left|\sum_{ij}\left(\int d^3r\phi_i(\mathbf{r})r_\nu\phi_j(\mathbf{r})\right)\sqrt{\epsilon_{ij}}F_{I,ij}\right|^2.$$

The computationally most expensive step is the compilation of the Coulomb term in the coupling matrix which scales $O(N^6)$, where N denotes the number of electrons. This scaling can be improved to $O(N^5)$ by calculating $v_{kl}(\mathbf{r}_1)=\int d^3r_2\,\phi_k(\mathbf{r}_2)\phi_l(\mathbf{r}_2)/|\mathbf{r}_2-\mathbf{r}_1|$ in k-space (note, that v_{kl} is the solution of the Poisson equation with a charge density $\phi_k\phi_l$) and than evaluate the integrals $\int d^3r_1, \phi_i(\mathbf{r})\phi_j(\mathbf{r})v_{kl}(\mathbf{r})$ for all particle-hole pairs ij.

3 The Optical and Photoelectron Spectra of Na Clusters

Optical and photoelectron spectroscopy[1] provides invaluable insights into the electronic structure, ionic configurations, thermal processes and dynamics in metal clusters, as well as about the size-dependent evolution of these properties. A comparison of the experimentally observed spectra and line-shapes with first-principle calculations contribute to a deeper understanding of these nanoscale systems. We show in this section that the photoabsorption cross sections, $\sigma(\omega)$, calculated via the TDLDA by averaging the oscillator strength f_I along finite-temperature BO-LSD-MD phase-space trajectories[8], provide a *quantitative ab-initio description* of the *absolute magnitudes, peak positions, and line shapes* of optical absorption spectra measured at various temperatures[15].

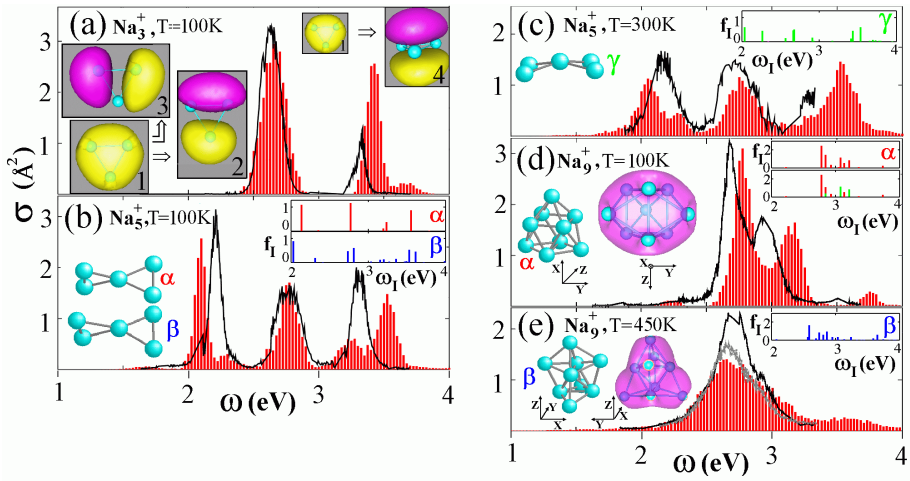

Figure 1. Theoretical (red histograms) and experimental[15] (black curves) photo absorption cross section for Na_3^+ at 100 K (a), Na_5^+ at 100 K (b) and 300 K (c), as well as for Na_9^+ at 100 K (d) and at 450 K (e). Grey insets in (a) display isosurfaces of the 4 lowest KS orbitals where yellow and purple distinguish the sign of the wave function and light blue spheres mark the position of the ions. The right top corner insets in (b-e) show static TDLDA spectra: (b) for the Na_5^+ GS (structure α), and for an instantaneous structure β with an elongated left triangle; (c) for an instantaneous bent planar geometry (γ). The calculated spectrum shown in (d) derives exclusively from configurations lying in the basin of the GS structure α whose oblate spheroidal electron density is depicted by the purple isosurface. The static spectrum of α is shown at the top inset in (d), and in the bottom inset we show the decomposition of that spectrum into the component along the z-axis (green sticks) and the perpendicular components (red sticks). The Na_9^+ isomer β is shown in (e), along with its electron density (purple isosurface) and its static spectrum (right top inset). To highlight the sensitivity of the experimental results to the temperature, we include in (e) the measured spectrum[15] at 540 K (grey curve).

Fig. 1 displays a comparison of the theoretical cross sections (red histograms) with the experiment spectra (black curves) of small sodium cluster cations. The calculated Na_3^+ spectrum at $T\approx$100 K (Fig. 1a) exhibits a low energy peak originating from two transitions $\omega_1^t=\omega_2^t\approx$2.65 eV, from the occupied s-like orbital to two empty p-like KS orbitals located in the plane of the Na_3^+ equilateral triangle (see grey insets 1, 2 and 3 at the left of Fig. 1a). The high energy peak at ω_3^t=3.41 eV is due to an excitation to another p-like orbital that is perpendicular to the cluster plane (grey inset 4 in Fig. 1a). In the experiments $\sigma(\omega)$ is determined from the depletion of the Na_n^+ intensity due to dissociation following absorption of a photon $\hbar\omega$. Excitation into the *in-plane* anti-bonding orbitals (insets 2 and 3) promotes such dissociation and is accompanied by exhaustion of the oscilator strength for the first (lower energy) measured peak. Excitation into the *out-of-plane* orbital (inset 4) has no direct destabilizing effect and consequently in the measurements only 66% of the Thomas-Reiche-Kuhn sum rule[12] is observed while the full sum rule is found in the theoretical spectrum shown in Fig. 1. Thermal motions distort the D_{3h} symmetry of the Na_3^+ ground state (GS) and the degeneracy of the low-energy transitions ω_1 and ω_2 is lifted resulting in a strong broadening of the first peak in Fig. 1a. An thermal activated breathing mode leads to an additional broadening of both peaks in Fig. 1a (see ref. 8 for more details).

Similarly, the finite temperature dynamics of Na_5^+ distorts (even at T=100 K) the optimal D_{2d} GS symmetry (see GS α in Fig. 1b where the perpendicular left and right triangles are equivalent, and compare to the instantaneous structure β shown in Fig. 1b with an elongated left triangle), resulting in fragmentation of the GS line at ω= 2.8 eV into two separate spectral lines. While the relatively moderate structural distortions occurring at 100 K are not sufficient to lift the degeneracy of the states associated with the low energy absorption line of Na_5^+ (at $\sim$2 eV, compare insets α and β at the upper right of Fig. 1b) which remains relatively sharp, increase of the temperature to 300 K results in bent configurations (see instantaneous structure γ on the left in Fig. 1c) where the low energy line is fragmented (see inset γ at the upper right of Fig. 1c), resulting in enhanced broadening of that spectral line (compare Figs. 1b and 1c).

For larger clusters, the occurrence of thermal isomerizations opens an additional line-broadening channel. The GS structure of the Na_9^+ cluster is shown at the left of Fig. 1d (marked α) and the TDLDA spectrum calculated for this static configuration exhibits several absorption lines distributed in a bimodal-like manner (see top inset at the upper right of Fig. 1d). This bimodality originates from the "oblate shape" of the cluster with radii R_z=2.68 Å along the D_{3h} symmetry axis (z in Fig. 1d) and R_{xy}=3.22 Å in the xy plane (these radii were determined from the diagonalized moment of inertia of the ionic GS structure α). The total electron density (see purple isosurface in Fig. 1d) is almost an ideal oblate spheroid. The bimodal character of the 100 K photoabsorption spectrum is evident in both the measured and calculated spectra (Fig. 1d), with further broadening caused by thermal motions through line-fragmentation and breathing vibrations of the cluster.

The main thermal effect in the spectra of Na_9^+ is the conversion of the low T (Fig. 1d) bimodal spectrum to one with a single broad maximum at higher temperatures (Fig. 1e). This change in the spectrum is caused mainly by transformations between the GS geometry (α, Fig. 1d) and the structural isomer β (see configuration on the left of Fig. 1e). The static spectrum of the β isomer is shifted to lower energies with respect to that of the GS (α) structure (compare top insets marked α and β at the upper right corners of Figs. 1d and 1e). Thus, the high-temperature broad spectral feature (Fig. 1e) may be described qualitatively as a thermal-weighted superposition of the spectra of the GS (α) and the structural isomer β, each broadened via thermal ionic motions about their free energy basins. The β-isomer may be characterized as having an octupolar shape, reflected in the shape of the electron density shown in Fig. 1e (see purple isosurface).

Similar effects can be observed in the photoelectron spectra (PES) of Na cluster anions[9]. A comparison of recently measured photoelectron spectra (PES) with the Gaussian broadened electronic density of states (DOS, i.e. a histogram of the KS energies ϵ_i) obtained from ab-initio calculations for T=0 K optimal structures (see Fig. 2 for the GS of sodium cluster anions with less than 20 atoms found by us employing BO-LSD-MD; for a discussion of the apparent growth patterns, the reader is refered to ref. 9) allows us to extract detailed information about the static properties of these simple metal clusters (see Fig. 3). For instance, our calculations revealed two degenerate GS isomers for Na_{12}^- and Na_{13}^-, respectively (see Fig. 2). However, after the inspecting the resulting DOS and the the experimental PES, the prolate isomers could be clearly ruled out (Fig. 3). A likely explanation for the preference of oblate Na_{12}^- and Na_{13}^- is that these clusters are formed by evaporation of monomers from the slighlty larger parent clusters (which are *oblate*, see Fig. 3) and thus still reflect the shapes of their parents.

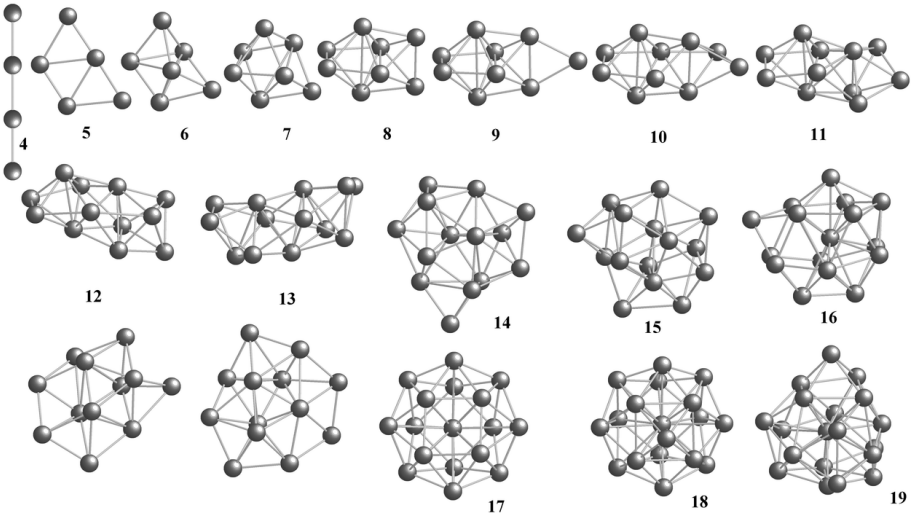

Figure 2. Ground state structures of Na_N^- clusters (N=4−19). For most sizes energetically close lying isomers were found. For Na_{12}^- and Na_{13}^-, two degenerate isomers with different shapes occur - those in the middle row are prolate, and those in the bottom row are oblate.

We saw already in case of the Na cluster cations, that finite temperature clusters undergo large amplitude vibrations or even isomerisation. In such a case also the PES represent superpositions of the spectra of more or less different configurations and therefore yield information about the isomerization dynamics. In addition to simple structural optimizations, we also performed extensive ab initio finite temperature (T=300 K) MD simulations extending over tens of picoseconds. Note, the overall improvment in the agreement between the simulated finite temperature spectra and the experiment in Fig. 3 justifying theoretical conclusion about the (experimentally not observable) cluster shapes (the reader is refered to ref. 9 for a detailed discussion of thermal effects in the spectra).

4 Relativistic Effects in Small Au Clusters

The atomic electronic structure of Cu, Ag, and Au, with a filled d-shell and a singly occupied s-shell [$nd^{10}(n+1)s^1$, with $n = 3, 4$ and 5 for Cu, Ag, and Au], suggests that the properties of these coinage metals could be treated to first approximation through the use of a "simple metal" framework – that is, as s^1-electron systems perturbed, with increasing strength from Cu to Au, by the underlying filled d-shell. However, the above view may be oversimplified since this series contains Au, which is the element known to exhibit the strongest relativistic effects among any atoms lighter than Fermium (Z=100)[16]. Indeed, manifestations of these effects are found throughout the physics and chemistry of gold in various forms and degrees of aggregation, from gold-containing small molecules to the optical properties of bulk gold and gold clusters[16].

Recently, there has been a surge of interest in the properties of finite nanoscale gold systems serving as building blocks of nanostructured materials and electronic devices, as

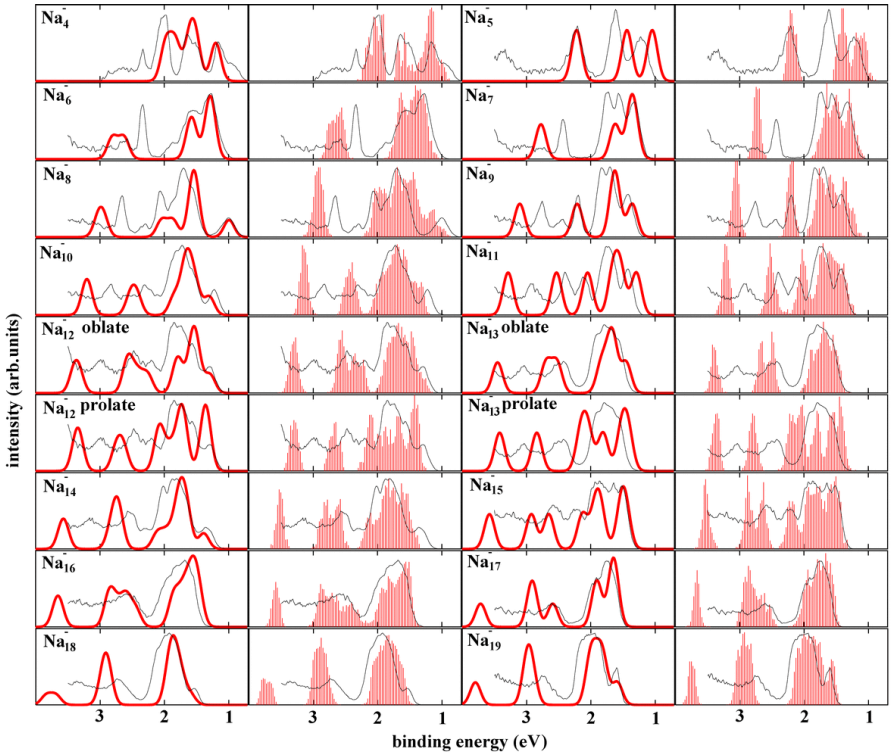

Figure 3. Experimental photoelectron spectra of sodium cluster anions (thin solid curves)[9] are compared to the Gaussian broadened (σ= 0.08 eV) ground state DOS (thick solid curves in the 1st and 3rd columns), and to the thermally broadened DOS obtained from room temperature BO-LSD-MD trajectories (histograms in the 2nd and 4th columns).

well as novel nanocatalytic systems[17]. In light of the above, and because of the observed extreme size sensitivity of the physical properties of small gold clusters, it is imperative to gain a fundamental understanding of their electronic and geometric structure, and put it in context within the coinage metal group. Added motivation for such studies derives recent gas-phase mobility experiments[18] where evidence has been found for 2D structures of Au_N^- with N extending up to 9-11.

Fig. 4 displays the results of an extensive density functional study of the heptamer anions Cu_7^-, Ag_7^-, and Au_7^-. Relativistic effects on bonding and structures in small gold clusters lead to quite remarkable results: the ground state structure and the energetically close-lying first isomer of Au_7^- are planar, separated by a large energy gap of 0.47 eV from the lowest-lying 3D isomer. Relativity can be switched off artificially in our density functional code by employing a non-relativistic pseudopotential. After doing so the 2D-3D ordering of the isomer changes making non-relativistic gold similar to the Ag and Cu case with 3D ground states. The propensity of anionic gold clusters to prefer planar structures continues up to surprisingly large sizes (possibly up to 13-14 atoms). This correlates with a relativistically-enhanced stronger sd hybridization in gold than in Ag and Cu, where for the latter elements the 2D-to-3D structural transition occurs for smaller clusters.

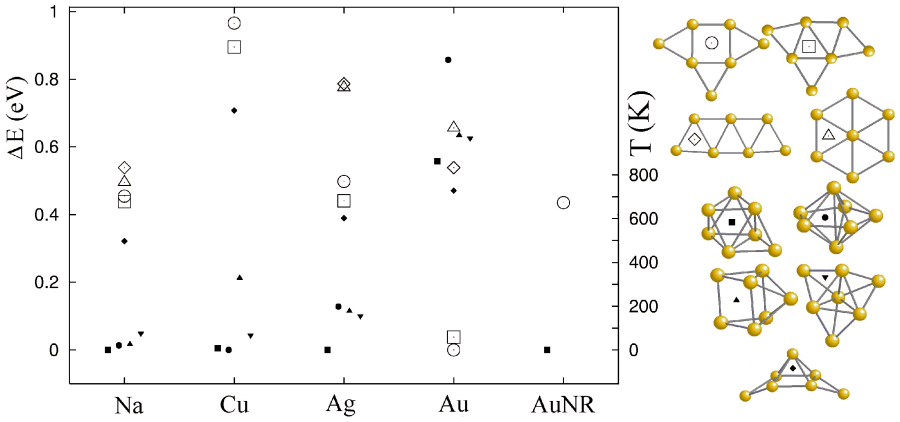

Figure 4. (a): Differences in total energy between the isomers and the ground-state structures of seven-atom anionic clusters of Na, Cu, Ag, and Au. Open and filled symbols denote 2D and 3D structures, respectively. The considered structures (9 per element) and assigned symbols are shown on the right hand side of the graph. "AuNR" denotes "non-relativistic gold".

5 Softlanding of Pd Clusters on MgO(001)

The scientific and industrial importance of transition metal particles on ceramics supports is based on their usage as catalysists in many applications like the cleaning of exhaust gases (i.e. the CO-NO reaction in car catalytic converters) or cyclomerization reactions in C-H chemistry[20]. Despite the broad interest in these systems little details are known concerning their structure and the pathways of the products in the catalised reactions. In this context a deeper theoretical understanding is surely usefull and could assist chemists in their attempts to improove existing catalytic components or to design new catalysts. Such an understanding requires the knowledge of the structures of the supported particles. Even the deposition dynamics might be of interest in order to clarify the presence or absence of coalescence and fragmentation processes during and after cluster deposition.

We performed extensive BO-LSD-MD simulations treating for the first time cluster soft-landing on an ab initio level finding the structures of Pd_2 to Pd_7 and Pd_{13} deposited on a realistic surface namely a MgO (001) with one oxygen vacancy. The MgO substrate with the F-center (FC) was modeled with a two-layer cluster $Mg_{13}O_{12}$, embedded into a lattice of point-charges in order to simulate the long-range Madelung potential.

The initial geometrical structures of the Pd_N clusters were taken from our recent gas-phase study[19]. The clusters were placed with a random orientation 4 Å above the FC (measured from the cluster atom closest to the surface) and an initial velocity directed perpendicular to the MgO surface, corresponding to a kinetic energy of 0.1 eV per atom to simulate softlanding conditions. Subsequent to the dynamical evaluation of the deposition process for about 1 ps the simulation was stopped, and starting from the last recorded configuration a corresponding potential energy minimum was located.

The adsorption of a single Pd atom on top of the FC (*t*FC site) is characterized by a strong binding energy (3.31 eV) and a short equilibrium adsorption distance (1.65 Å),

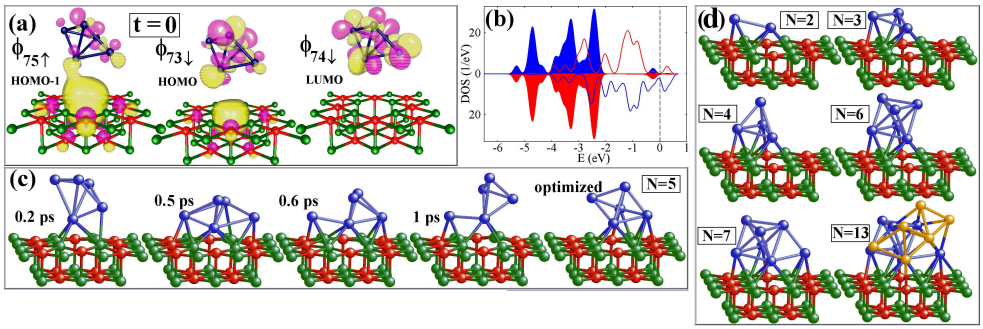

Figure 5. A Pd_5 cluster impinges with 0.1 eV/atom kinetic energy on an F-center in a MgO (001) surface. Pd atoms are depicted as blue, Mg as green and O as red spheres. (a) Isosurfaces of the highest occupied up-spin molecular orbital (HOMO-1), the highest occupied down-spin orbital (HOMO) and the lowest unoccupied down-spin orbital (LUMO) of the initial configuration at t=0 (color coding distinguishes the sign of the wave function). Note, that the 75 up-spin and 73 down-spin orbitals are both occupied. (b) The corresponding local densities of states of the surface (blue area for up- and red area for the down-spin DOS) and of the cluster (red line for up- and blue line for down-spin DOS). The Fermi level, $E_F = 0$. We note that the DOS of the isolated surface and free cluster are essentially identical to that shown here, except for the first peak below E_F that corresponds to the long-range interaction discussed in the text. (c) Snapshots from the MD simulation recorded at the indicated times. (d) GS structures of Pd_N (N=2,3,4,6,7 and 13). Color coding as in (a) except for Pd_{13} where a subset of the Pd atoms is colored in yellow in order to highlight the Pd_7 subunit (blue).

compared to adsorption on-top of an oxygen (*t*O) atom at the ideal MgO surface (1.16 eV and 2.17 Å). The bonding between the Pd atom and the FC involves the localized FC electronic orbital, located in the band gap of MgO (separated from the top of the valence band by 2.3 eV), and (mainly) the $d(m = 0)$ orbital of the Pd atom. The attractive interaction to the F-center is rather long-ranged extending up to about 5 Å above the surface; e.g., the interaction energy of a Pd atom placed 5.2 Å above the FC is 0.1 eV. This weak attraction is due to polarization of the d(m=0) valence orbital of Pd by the FC.

We conclude that the F-center acts as a rather wide attractive "funnel" for the Pd atom, extending several Å both laterally and vertically. This funneling effect steers the incident cluster and dominates the dynamics of the initial phases of the deposition process, as illustrated in the following for the representative case of a Pd_5 cluster.

When the Pd_5 cluster is placed 4 Å above the oxygen vacancy, the FC electronic state (located just below E_F) combines with d-orbitals of the closest Pd atom to form two bonding molecular orbitals (see the up-spin HOMO-1 and the down-spin HOMO in Fig. 5a). All other orbitals (for example the lowest unoccupied orbital (LUMO) of Pd_5 shown in Fig. 5a) remain to a large degree eigenstates of the separated systems, and consequently the corresponding density of states (DOS in Fig. 5b) may be represented as a superposition of those of the bare surface and the gas-phase cluster.

The long-range attraction between the cluster and the FC accelerates the lowermost Pd atom towards the *t*FC site (note the strong deformation of the Pd_5 cluster at 0.2 ps in Fig. 5c). Subsequently, other Pd atoms are attracted to neighboring MgO bridge positions (Fig. 5c, t=0.5 ps) accompanied by additional release of kinetic energy.

Optimization of the adsorbed cluster after roughly 1 ps MD simulation resulted in a trigonal bipyramide structure (which coincides with the gas-phase optimal configuration)

lying with a triangular facet against a *t*FC-MgObridge-MgObridge surface triangle.

Using the above-mentioned methodology, we have determined the ground-states for the other deposited Pd_N clusters. For $3 \leq N \leq 6$ we observed a regular structural size evolution (Fig. 5d) where the gas-phase ground state structures are anchored to the MgO surface with one Pd atom on the *t*FC, another Pd on MgMgO hollow site (for $N = 2$) or 2 additional Pd atoms on MgO bridge sites (for $3 \leq N \leq 6$). However, for Pd_7 and Pd_{13} the free clusters transform to structures that exhibit a higher degree of commensurability with the underlying surface, incorporating a Pd_6 and Pd_7 subunit, respectively (Fig. 5d). In this case, the loss in the intracluster cohesion is counterbalanced by a considerable gain of adhesion energy marking the beginning of surface wetting.

6 Conclusion and Outlook

The interplay between experiment and large scale ab initio simulations provides a deeper understanding of free and supported clusters as demonstrated in this paper for simple metal as well as the more complicated coinage metal clusters. In future, we will proceed to larger cluster sizes and study for instance relativistic effects in gold nanocristals or the influence of passivating ad-molecules. Furthermore, we will continue with the study of supported Pd clusters by looking at reactions on these nano-sized catalysts.

References

1. W. deHeer, Rev. Mod. Phys. **65**, 611 (1993).
2. C.Brabec et al., Adv. Funct. Mater. **11**, 15 (2001).
3. *Metal Clusters at Surfaces*, ed. K.H.Meiwes-Broer (Springer, Berlin, 2000).
4. M.Moseler, H.Häkkinen and U.Landman, Phys. Rev. Lett. **89**, 176103 (2002).
5. W.Kohn and L.J.Sham, Phys. Rev. A **140**, 1133, (1965).
6. R.Parr and W.Yang, *DFT of atoms and molecules* (Oxford university press, 1989).
7. R.Barnett and U.Landman, Phys. Rev. B **48**, 2081 (1993).
8. M.Moseler, H.Häkkinen and U.Landman, Phys. Rev. Lett. **87**, 053401 (2001).
9. M.Moseler, et al, Phys. Rev. B (accepted).
10. H.Häkkinen, M.Moseler and Uzi Landman, Phys. Rev. Lett. **89**, 033401 (2002).
11. E. K.U. Gross et al., in Topics in Current Chemistry, edited by J. D. Dunitz et al. (1990), Vol. 181, pp. 81171.
12. M.E.Casida, in: Recent Advances in DFT Methods, ed. D.P.Chong (Singapore: World Scientific), p. 155-192.
13. N.Troullier, and J.L.Martins, Phys. Rev. B **43**, 1993 (1991).
14. J.P.Perdew et al., Phys. Rev. Lett. 77, 3865 (1996).
15. M.Schmidt et al., Phys. Rev. B **59**, 10970 (1999).
16. P. Pyykkö, Chem. Rev. **88**, 563 (1988).
17. A. Sanchez et al., J. Phys. Chem. A **103**, 9573 (1999).
18. Furche et al., J. Chem. Phys. **117**, 6982 (2002).
19. M.Moseler, H.Häkkinen, R.Barnett, U.Landman, Phys. Rev. Lett, **86**, 2545 (2001).
20. U.Heiz and W-D.Schneider, in ref. 3.